1 **Warm and Moist Air Intrusions into Winter Arctic: A Lagrangian view on the near-surface energy budgets**

2 Cheng You[1], Michael Tjernström[1], Abhay Devasthale[2]

3 [1]Department of Meteorology & Bolin Centre for Climate Research, Stockholm University, Stockholm, Sweden.

4 [2]Remote Sensing Unit, Research and Development Department, Swedish Meteorological and Hydrological
5 Institute, Norrköping, Sweden.

7 *Correspondence to*: Cheng You (cheng.you@misu.su.se)

8 **Abstract**. In this study, warm and moist air intrusions (WaMAI) over the Arctic Ocean sectors of Barents, Kara,
9 Laptev, East Siberian, Chukchi and Beaufort Seas in recent 40 winters (from 1979 to 2018) are identified from
10 ERA5 reanalysis using both Eulerian and Lagrangian views. The analysis shows that WaMAIs, fuelled by Arctic
11 blockings, causes a relative surface warming and hence a sea ice reduction by exerting positive anomalies of net
12 thermal irradiances and turbulent fluxes to the surface. Over Arctic Ocean sectors with land-locked sea ice in
13 winter, such as Laptev, East Siberian, Chukchi and Beaufort Seas, total surface energy budget is dominated by
14 net thermal irradiance. From a Lagrangian perspective, total water path (TWP) increases linearly with the
15 downstream distance from the sea ice edge over the completely ice-covered sectors, inducing almost linearly
16 increasing net thermal irradiance and total surface energy-budget. However, over the Barents Sea, with an open
17 ocean to the south, total net surface energy-budget is dominated by the surface turbulent flux. With the energy in
18 the warm-and-moist air continuously transported to the surface, net surface turbulent flux gradually decreases
19 with distance, especially within the first 2 degrees north of the ice edge, inducing a decreasing but still positive
20 total surface energy budget. The boundary-layer energy-budget patterns over the Barents Sea can be categorized
21 into three classes: radiation-dominated, turbulence-dominated and turbulence-dominated with cold dome,
22 comprising about 52%, 40% and 8% of all WaMAIs, respectively. Statistically, turbulence-dominated cases with
23 or without cold dome occur along with one order of magnitude larger large-scale subsidence than the radiation-
24 dominated cases. For the turbulence-dominated category, larger turbulent fluxes are exerted to the surface,
25 probably because of stronger wind shear. In radiation-dominated WaMAIs, stratocumulus develops more strongly
26 and triggers intensive cloud-top radiative cooling and related buoyant mixing that extends from cloud top to the
27 surface, inducing a thicker well-mixed layer under the cloud. With the existence of cold dome, fewer liquid water
28 clouds were formed and less or even negative turbulent fluxes could reach the surface.

29 Keywords: Arctic climate, Stratocumulus, Trajectories, Warm and moist air intrusions

30 **1. Introduction**

31 In recent decades, rapidly intensified Arctic warming has been observed (Cohen et al., 2014; Graversen et al.,
32 2008a; Screen et al., 2018), which has become known as Arctic amplification (Serreze and Francis 2006).
33 Accompanying this warming has been a dramatic melting of Arctic sea ice (Screen and Simmonds, 2010;
34 Simmonds, 2015; Simmonds and Li, 2021). Particularly over the Barents Sea, a rapid warming rate, as well as a
35 remarkable sea ice decrease, is found, which may have impacts on the extreme cold winters in Eurasia (Kim et
36 al., 2014; Kim and Son, 2016; Li et al., 2021; Luo et al., 2019; Mori et al., 2014; Overland et al., 2011; Petoukhov
37 and Semenov, 2010; Rudeva and Simmonds, 2021; Tang et al., 2013).

38 Arctic amplification is likely a consequence of many contributing processes and a detailed attribution to different
39 factors is yet to be performed. The most commonly implied mechanism is the so-called albedo feedback, based
40 on the consideration that open water absorbs considerably more solar radiations than sea ice, which would
41 accelerate Arctic warming (Kim et al., 2019). However, Arctic amplification is the strongest in winter, when the
42 sun is mostly absent and the albedo by definition plays no role at all. This suggests that atmospheric energy
43 transport by warm-and-moist intrusions (WaMAI) may play an important role for Arctic amplification, especially
44 in winter. The positive trend in number of winter WaMAIs can statistically explain a substantial part of the surface
45 air temperature and sea-ice concentration trends in the Barents Sea (Luo et al., 2017a; Nygård et al., 2020; Woods
46 and Caballero, 2016).

47 Most of these studies deal with winter and focus either on the dynamical mechanisms resulting in WaMAIs, or on
48 the effects of WaMAIs on the Arctic climate system conducted from an Eulerian perspective by retrieving
49 composite mean of WaMAIs properties (Liu et al., 2018), or calculating regressions between different metrics
50 (Gong and Luo, 2017). In recent years it has been increasingly argued that the concept of Lagrangian air mass
51 transformation is necessary for studying WaMAIs (Ali and Pithan, 2020; Komatsu et al., 2018; Pithan et al., 2018).
52 Trajectories have been utilized to study the origin and transport pathway of winter WaMAIs (Papritz et al., 2022),
53 as well as the thermodynamic processes along the trajectories (Papritz, 2020). A method using trajectories to
54 analyze WaMAIs from a Lagrangian perspective was designed by You et al. (2020) and tested on a summer
55 WaMAI event described in Tjernström et al. (2015). This method was utilized to build a climatology of summer
56 WaMAIs (You et al., 2021).

57 In this paper, we use this method to explore winter WaMAIs over several sectors of the Arctic Oceans: the Barents,
58 Kara, Laptev, East Siberian, Chukchi and Beaufort Seas. Over the Barents Sea, sea ice concentration is decreasing
59 and the near-surface atmosphere south of the ice edge is heated by comparatively warm open water. In contrast,
60 for the Laptev, East Siberian, Chukchi and Beaufort Seas, the ocean surface is almost completely frozen to the
61 coast and the insulation effect by sea ice suppresses heat transfer between ocean and atmosphere. We will attempt
62 understanding the distinctions between the ocean sector with open water and those with land-locked sea ice by
63 comparing surface and boundary-layer energy-budgets from both Eulerian and Lagrangian perspectives.

64 **2. Data and method**

65 **2.1 Data**

66 We use the latest reanalysis from European Centre for Medium-Range Weather Forecast (ECMWF), ERA5
67 (Hersbach et al., 2020) in this study. For the detection and Eulerian analysis of WaMAIs in recent 40 winters (DJF
68 from 1979 to 2018), we use the reanalysis dataset at a 6-hourly temporal and 0.75° horizontal resolution. This
69 includes the vertically integrated northward water vapor flux (f_w), sea ice concentration (SIC), 500-hPa
70 geopotential height (GH$_{500}$), 2m air temperature (T_{2m}), 850-hPa temperature (T_{850}), total water path (TWP),
71 liquid water path (LWP), ice water path (IWP) and precipitation rate (PRCP). For the Lagrangian analysis we also
72 use ERA5 3D wind field at a 6-hourly resolution for the calculations of air-mass trajectories during WaMAIs, in
73 the same way as described in You et al. (2020, 2021). We additionally interpolate energy-budget terms with
74 forecast data from ERA5 at the higher temporal resolution (1-hourly). This includes surface net solar (F_{sw}) and

75 thermal (F_{lw}) irradiances, the surface sensible (F_{sh}) and latent heat fluxes (F_{lh}), as well as the 1-hourly temperature

76 tendencies due to different model physics extracted at model levels.

77 Utilizing ERA5 reanalysis introduces uncertainty, especially for anything that comes from parameterized

78 model physics such as cloud parameters and the energy budget. Large upward residual heat flux biases exist

79 among all reanalysis and turbulent heat flux over the sea ice are also poorly simulated in all seasons (Graham et

80 al., 2019). ERA5 has larger warm bias in winter, especially when the surface temperature is under $-25°C$. Sea

81 ice thickness is thinner in ERA5 because of the larger warm bias and higher precipitation (Wang et al., 2019). In

82 the data assimilation, the main variables in a reanalysis are constrained by observations and in-situ observations

83 over the central Arctic Ocean are sparse, especially in winter. The loss of all visible wavelengths in passive remote

84 sensing in winter also makes many satellite products less trustworthy. However ERA-Interim, the predecessor of

85 ERA5, generally performs best among the available reanalysis datasets, especially for the wind (Lindsay et al.,

86 2014) and ~~-~~ substantial progress has been made in data quality and diagnostic techniques during last few decades

87 (Mayer et al., 2019). However, it would be not possible to analyze air mass transformation climatologically on

88 the energy-budgets along the trajectories of winter WaMAIs in any other way than relying on reanalysis. Here,

89 we alleviate uncertainty in two ways; first, by averaging over a large number of cases and second, by considering

90 anomalies rather than actual mean values. Avoiding single case studies reduces random errors, while considering

91 anomalies reduces systematic errors.

92 **2.2. WaMAI Detection**

93 Clouds and moisture are integral and important parts of the Arctic surface and boundary-layer energy budgets and

94 relative humidity in the Arctic boundary layer is almost always high (Andreas et al., 2002; Persson et al., 2002).

95 ~~Although it is possible to have a warm and dry air mass intruding in the Arctic, it is quite unlikely to have an~~

96 ~~intrusion that is moist and cold~~ A particular warm air intrusion may carry less moisture than a typical moist

97 intrusion, but a typical moist intrusion will certainly carry warm air into the Arctic. We therefore name

98 these events as 'warm and moist air intrusions', ~~-~~ identify and quantify them ~~WaMAIs~~ with ~~by analyzing~~ the

99 vertically integrated northward moisture flux, f_w, separately over the ocean sectors of Barents, Kara, Laptev, East

100 Siberian, Chukchi and Beaufort Seas (Figure 1). Among these sectors, winter SIC only varies substantially with

101 the time over the Barents and Kara Seas. North of $80°N$ in the Barents Sea, SIC has a statistically significant

102 regression coefficient ~~correlation~~ with f_w (Figure 2a). locations that pass a $p < 0.05$ Student's t-test (stippled in

103 Figure 2a) are considered the sensitive region. For the remaining sectors, all sea ice covered locations are

104 considered sensitive regions since they do not display winter variability in SIC. The mean f_w over each sensitive

105 region, $\overline{f_w}$, are approximately normally distributed (Figure 2b and d). We define a WaMAI as a continuous period

106 when $\overline{f_w} > 0$ (red lines in Figure 2c and e) with a maximum larger than the 95-percentile of the distribution of all

107 values of $\overline{f_w}$. The portion of a WaMAIs when $\overline{f_w}$ is larger than the 95-percentile are moreover considered extreme

108 moist intrusions (EMIs; blue line in Figure 2c and e); note that each WaMAI can only include one EMI. The onset

109 and terminal time of a WaMAI is taken at the nearest minimum values of $\overline{f_w}$, or zero of $\overline{f_w}$.

110 Similar as You et al.(2021, 2020), ensembles of two day forward and backward trajectories at different

111 altitudes are calculated for each WaMAI over all ocean basins, using the trajectory algorithm from Woods et al.

112 (2013). Over each ocean sectors and for each WaMAI, we select a launch point along a latitude circle where the

113 T850 is the largest. The latitude circle of 75 °N (blue lines in figure 2a) is used for all ocean sectors, except for
114 the Barents Sea where 80 °N (red line in figure 2a) is used. Forward (backward) trajectories are also terminated
115 where they start to track southward (northward). Hence, we only capture the part of each trajectory that
116 continuously tracks northwards. Finally, the terminal points of selected trajectories have to be at least 5° north of
117 the sea-ice edge, defined as where SIC exceeds 15% and reach 80 °N (85 °N for the Barents Sea sector).
118 Trajectories are calculated at several different heights, every 100 m, from 300 m to 800 m and vertical profiles of
119 the various variables are then extracted from ERA5, from the surface to 2 km, by interpolation in time and space
120 along each of these trajectories. The final vertical cross-section for each WaMAI is the ensemble average of the
121 results along all trajectories initialised at different heights. For the 40 winters in this study, 87 (131) WaMAIs are
122 detected over the ocean sectors with open ocean (land-locked sea ice) for a total of 218 WaMAIs.

123   It is to be noted that both the temporal and spatial resolutions would influence the accuracy of the
124 trajectory calculation (Stohl et al., 1995). However, the increase of only temporal or spatial resolution does not
125 necessarily improve the accuracy of trajectory calculation (Draxler, 1987). In this study, we calculate the
126 trajectories 2 days forward and backward, instead of calculating 4 days trajectory at once. Furthermore, we also
127 calculate the ensembles of trajectories at different heights to decrease the error introduced by vertical interpolation
128 from pressure level to geometric height.

129

130 **2.3. Energy Budgets**

131 As shown in Eq. 1, total surface energy-budget (F_{total}) is contributed by surface net solar irradiance (F_{sw}), surface
132 net thermal irradiance (F_{lw}), surface turbulent sensible heat fluxes (F_{sh}) and surface turbulent latent heat fluxes
133 (F_{lh}). Note that all surface net energy fluxes contributing to a surface warming are considered positive. Individual
134 terms in Eq. 1 are also interpolated from ERA5 at each 0.5-degree interval in latitude along the trajectories.

135 $$F_{total} = F_{sw} + F_{lw} + F_{sh} + F_{lh} \quad (1)$$

136 We also evaluate the cloud longwave radiative effects (CRE) ($F_{lw\_CRE} = F_{lw\_all\_sky} - F_{lw\_clear\_sky}$), using the
137 same method. $F_{lw\_all\_sky}$ is the surface net thermal irradiance, considering the actual clouds presence, while
138 $F_{lw\_clear\_sky}$ is clear-sky counterpart, assuming clouds were not present.

139 For the atmospheric energy budget calculations, we also extract the temperature tendencies due to different model
140 physics from ERA5, where we can resolve all terms in the thermal equation (Eq. 2). As shown in Eq. 2, the total
141 temperature tendency T_t of an air-mass in a WaMAI is contributed by heating/cooling from the divergence of
142 shortwave irradiance ($\frac{\partial T}{\partial t}_{sw}$), longwave irradiance ($\frac{\partial T}{\partial t}_{lw}$) and vertical turbulent heat flux ($\frac{\partial T}{\partial t}_{TH}$) and the latent heat
143 of condensation in cloud formation ($\frac{\partial T}{\partial t}_{LH}$). In a Lagrangian view, the advection tendencies are by definition zero,
144 while in an Eulerian view, the total tendencies would additionally be balanced by temperature advection. All these
145 terms are also interpolated along the trajectories as previously discussed (also see You et al. 2020, 2021).

146 $$T_t = \frac{\partial T}{\partial t}_{sw} + \frac{\partial T}{\partial t}_{lw} + \frac{\partial T}{\partial t}_{LH} + \frac{\partial T}{\partial t}_{TH} \quad (2)$$

147 Note that while the surface energy budget depends on the surface fluxes, the atmospheric energy budget depends
148 on the vertical gradient of fluxes.

149

150

151 **3. Results**

152 **3.1 Large-scale Features**

153 EMIs were identified in the Arctic ocean basins of Barents, Kara, Laptev, East Siberian, Chukchi and Beaufort.
154 Figure 3 (4) shows the composite of all EMIs over the Barents (Beaufort) Sea, representing the large-scale features
155 of winter EMIs over ocean sectors with open ocean (land-locked sea ice). Both figure 3a and 4a show one pair of
156 negative and positive GH_{500} anomalies with a large geopotential height gradient in between, generating an
157 intensive f_w anomaly directed into the Arctic (Figure 3c, 4c), enhancing temperature advection (Figure 3b, 4b) and
158 cloud formation (Figure 3d, 4d), consistent with previous studies (Tjernström et al. 2015; Overland and Wang
159 2016; Gong and Luo 2017; Johansson et al., 2017; Sedlar and Tjernström 2017; Messori et al. 2018; Cox et al.
160 2019; You et al., 2021). Unlike over the Barents Sea, where the TWP anomaly is dominated by LWP (Figure 4d
161 and 4e), TWP over the Beaufort Sea is dominated by IWP. These features in the GH_{500}, T_{850} and TWP anomalies
162 are also found in all other ocean basins (Figure S1, S3, S5, S7).

163 As warm and moist air is advected into the Arctic over the Barents Sea, it interacts with the cool ice
164 surface through turbulence and radiation, enforcing positive F_{sh}, F_{lh} and F_{lw} anomalies at the surface (Figure 5c,
165 5d and 5e). The F_{sh} anomaly reaches > 60 W m^{-2} over open water near the Norwegian coast, tapering off northward
166 over the ice all the way to the pole. The pattern of F_{lh} anomaly is similar to that of F_{sh} south of 80°N, but decreases
167 to nearly zero over the sea ice north of 80°N. Positive LWP and IWP anomalies in figure 3d and 3e, extending
168 from the coast to the north pole along the path of the EMIs, also affects the surface energy-budget with a positive
169 F_{lw} anomaly (Figure 5c). This relation between F_{lw} anomaly and winter EMIs over the Barents Sea is also
170 discussed in other climatological analyses (Gong et al., 2017; Gong and Luo, 2017). In total, these anomalies in
171 the surface-energy fluxes sum up to a positive F_{total} anomaly, inducing decreased SIC (Figure 5b).

172 Similar surface energy-budget pattern is also found over the Beaufort Sea (Figure 6) and other ocean
173 sectors with land-locked sea ice (Figure S2, S4, S6, S8), but with some differences. The anomaly in F_{total} over the
174 Barents Sea is dominated by F_{sh}, while F_{total} anomaly over the Beaufort Sea is dominated by F_{lw}. The magnitudes
175 of F_{sh}, F_{lh} and F_{total} anomalies over the Beaufort Sea are less half the magnitude of those over the Barents Sea,
176 especially south of 80°N and hence induce four times less SIC decrease. As EMIs occur over the Beaufort Sea,
177 positive F_{sh}, F_{lh}, F_{total}, F_{lw}, LWP and IWP anomalies and negative SIC anomaly is found. However, negative F_{sh},
178 F_{lh}, F_{total}, F_{lw}, LWP and IWP anomalies and positive SIC anomalies could also be found over the Barents Sea
179 sector, while some WaMAIs from the Beaufort Sea pass through the pole and become cold spells over the Barents
180 Sea (Figure 4 and 6).

181 Table 1 summarizes the averaged surface energy-budgets over sea ice across the six basins. Except for
182 the Barents Sea, F_{lw} anomalies are almost twice larger than F_{sh} anomalies. Since F_{sw} anomalies can be ignored
183 in winter, the F_{lw} anomalies dominate F_{total}. However, over the Barents Sea, F_{sh} anomalies are almost twice larger

184 than F_{lw} anomalies and contribute to more than 50% of F_{total} anomalies. Over the Barents and Chukchi Sea,
185 positive F_{sh} anomalies are statistically significant, which is not the case for any of the other sectors. Except for
186 the Laptev Sea, positive F_{total} and F_{lw} anomalies are statistically significant. Here, if the mean values of these
187 surface energy-budget terms are positive and greater than their standard deviation, then we consider they are
188 statistically significantly positive.

189 The composites of large-scale pattern discussed above are extracted from the stronger EMI events to
190 generate a clear signal, however, these may not necessarily represent the general pattern of all WaMAIs. Therefore,
191 linear regressions of daily averaged GH, T_{850}, SIC, $F_{total,}$ F_{sh}, F_{lh}, F_{sw} and F_{lw} anomaly against the time series of
192 daily averaged $\bar{f}_w$ over the sensitive regions in recent 40 winters were calculated separately for all the examined
193 ocean basins. All the regressed fields have similar pattern as their counterparts in Figures 3~6, implying a similar
194 relationship for all days but at smaller magnitudes. Since the regressions confirm the conclusions, we will consider
195 only the Barents and Beaufort Seas as an example of ocean sector with open ocean and land-locked sea ice,
196 respectively (Figure 7 and 8).

197

198 **3.2 The Surface Energy-budget**

199 In this section, we will explore the transformation of temperature inversion, cloud formation and surface energy-
200 budget along the trajectories of warm-and-moist air masses over ocean basins with open water and land-locked
201 sea ice, respectively, by compositing the heights to the maximum specific humidity (h_{sh}), temperature (h_t) and
202 vertical temperature gradient (h_{t_z}), along with TWP, LWP, IWP, precipitation rate (PRCR) and surface energy-
203 budget terms (F_{sh}, F_{lh}, F_{total}, F_{lw}) from all detected WaMAIs.

204 Over the completely ice-covered sea sectors such as the Laptev, East Siberia, Chukchi and Beaufort Seas,
205 strong temperature inversion develops with cloud formation below, as the warm-and-moist air propagates over
206 the sea ice. In this case, h_{sh} is higher than h_t, and both are higher than h_{t_z} (Figure 9a). From the ice edge and
207 onward up to 10 degrees north of the ice edge, $h_{sh,}$ h_t and h_{t_z} increase almost linearly, by 30-40 m per degree
208 latitude (Figure 9a) as the inversion is lifted. TCW and PRCP also increase northward, although more slowly for
209 the first two degrees, in total by 6 g m^{-2} and 0.4 mm day^{-1} per degree latitude, respectively, implying that
210 stratocumulus develop continuously along the trajectories (Figure 9b, c). The increasing TWP is mainly due to
211 the increase in IWP since LWP is almost constant along the trajectories (Figure 9b). The increase of h_{t_z} is
212 comparable to that of summer WaMAIs, while the increase in TWP is about half of that of summer WaMAIs
213 (You et al., 2021), since less moisture is available for cloud development in winter (Figure 4c). The gradual
214 increase of h_{t_z}, a manifestation of increased boundary-layer mixing, leads to a reduction in near-surface gradients.
215 Since the turbulent heat fluxes at the surface depend on these gradients, the F_{sh} anomaly decreases gradually at a
216 rate of 1.5 W m^{-2} per degree latitude (Figure 10a). Simultaneously, the F_{lw} anomaly increases almost linearly by
217 2.5 W m^{-2} per degree latitude, while F_{lh}, the smallest contributor to F_{total}, is almost constant along the trajectories
218 (Figure 10a). The increase in F_{lw} along trajectories is due to an increasing cloud radiative effects by the evolving
219 stratocumulus clouds; F_{lw_CRE} increases at a similar rate as F_{lw} (Figure 10b). From 0 to 2 degrees north of the sea
220 ice edge, the F_{total} anomaly is dominated by the F_{sh} anomaly, while farther north it is dominated by F_{lw} anomaly

221 (Figure 10a). Generally, F_{total} anomaly increases with the distance from the sea ice edge at a rate of 1 W m^{-2}

222 (degree latitude)$^{-1}$ and this increasing trend is dominated by F_{lw} anomaly (Figure 10a).

223   Over the Barents Sea, with open warm water south of the ice edge, h_t and h_{sh} also increase nearly linearly

224 but at a 1.6 times larger rate than those over ocean sectors with land-locked sea ice, however, starting at

225 considerably smaller values (Figure 9d). The maximum values of h_t and h_{sp} here are comparable to the minimum

226 values over the completely ice-covered sectors, implying that WaMAIs over the Barents Sea develops a shallower

227 well-mixed layer and hence bring the moist and warm air closer to the surface. However, the temperature inversion

228 over the Barents Sea is too weak to be easily identified with the metrics used above. Unlike for the sectors with

229 land-locked sea ice, TWP and PRCR are constant with downwind distance from the ice edge, varying slightly

230 around 150 g m^{-2} and 7 mm day^{-1} (Figure 9e, f). As a consequence, F_{lw} anomaly and F_{lw_CRE} along the trajectories

231 (Figure 10c, d) are nearly constant with northward distance. Although TWP remains quasi-constant, LWP (IWP)

232 decreases (increases) at a rate of -6 g m^{-2} (+6 g m^{-2}) along the trajectories (Figure 9e). From 0 to 4 degrees north

233 of the sea ice edge, TWP is contributed by LWP and IWP in about equal parts, while from 4 degrees north of the

234 sea ice edge and onward, TWP gradually becomes dominated by IWP. The F_{sh} anomaly decreases fast by nearly

235 50% over the first two degrees from the sea ice edge (Figure 10c). From 2 to 10 degrees north of the sea ice edge,

236 the decrease is more moderate at a rate of 4 W m^{-2} per degree latitude (Figure 10c), which is still faster than that

237 over the completely frozen ocean sectors. However, the F_{sh} anomaly is still larger than the largest corresponding

238 value for the completely frozen ocean sectors, even ten degrees north of the ice edge (Figure 10a). This is likely

239 due to the much warmer upstream conditions over the open ocean. The large thermal contrast between open ocean

240 and sea ice surface contributes to the stable atmospheric layer over the sea ice surface and rapidly reducing F_{sh}

241 anomaly, while the decrease of F_{sh} anomaly with downstream distance is due to the slowly reducing temperature

242 gradient resulting from the turbulent mixing. Similar decreasing trends are also present for F_{lh} and F_{total} anomaly

243 (Figure 10c). From 2 to 10 degrees north of the sea ice edge, they decrease at a rate of 1 and 5 W m^{-2} per degree

244 latitude, respectively (Figure 10c). Within 5 degrees north of the sea ice edge, F_{total} anomaly is dominated by F_{sh},

245 while downstream the turbulent heat flux ($F_{sh} + F_{lh}$) anomaly becomes comparable to F_{lw} anomaly and contribute

246 almost equally to F_{total} anomaly (Figure 10c).

247   Without the presence of solar radiation in winter, the variation of F_{total} anomaly over the Barents Sea is

248 dominated by F_{sh} anomaly (Figure 10a), while it is dominated by F_{lw} anomaly over ocean sectors with land-locked

249 sea ice (Figure 10c). This distinction between ocean sectors with and without open ocean upstream can be

250 explained by the stronger air-sea interaction over the Barents Sea (Kim et al., 2019). Before the air-mass is

251 advected in over the sea ice, it is heated and moistened by the ocean and consequently, exerts greater turbulent

252 heat fluxes to the surface as it suddenly enters over the sea ice (Figure 10c). Cloud formation happens already

253 upstream over the warm water and in a much deeper PBL and is hence not much affected by the advection over

254 sea ice. Instead a much shallower well-mixed layer forms as the air enters over the ice, and the larger vertical

255 gradients resulting from the large temperature difference across the ice edge gives rise to larger F_{sh}. This

256 dominance of turbulent heat fluxes remains until the halfway along the trajectories.

257 **3.3 The Boundary-layer Energy-budget**

As discussed in previous sections, cloud formation as part of the air-mass transmission can exert large variability on the surface energy-budget. Here, we focus on the cloud effects on the boundary-layer energy-budget. For each WaMAI, the boundary-layer energy-budget terms are evaluated and interpolated along the trajectory and analyzed on a case-by-case basis, categorizing patterns into four main categories: a) lifting temperature inversion (INV); b) radiation-dominated (RAD); c) turbulence-dominated (TBL); and d) turbulence-dominated with cold dome (TCD). Some typical cases are shown in figure 11-14 respectively for these four categories, illustrating different boundary-layer energy-budgets in each category, while conceptual summary graphs of all the different categories are summarized in Figure 15. The boundary-layer energy-budget pattern plotted this way is very variable from case to case, mainly because the northward component of the advection is differently from case to case; also, the location of the ice edge is different from year to year. Hence, some trajectories are long but reach less far north while other are shorter and still reaches further north. In the vertical, the cases are also subject to different subsidence, affecting the PBL growth. We therefore have yet to come up with a workable normalization that would allow an ensemble average of all the cases.

~~All ocean sectors fall within either of these, except for the Kara Sea that has some sea ice variability and open ocean. Hence, some WaMAIs behave as typical for the Barents Sea, while most behave like for the other sectors with land-locked sea ice.~~ Almost all WaMAIs over ocean sectors with land-locked sea ice feature a boundary-layer energy-budget pattern of category INV. Similar to category TBL for summer WaMAIs (You et al., 2021), category INV is characterized by increasingly lifting temperature inversion and continuously stratocumulus development near the inversion. Different from the ocean sectors with land-locked sea ice, clouds during WaMAIs over the ocean sector with an upstream open ocean (e.g. Barents Sea) form at the altitude of ~1 km, above the warm-and-moist air-masses. The boundary-layer energy-budget here is categorized into three categories (RAD, TBL, TCD). Category RAD is characterized by stronger cloud-top radiative cooling and related buoyant mixing, while category TBL is characterized by more intensive surface turbulent mixing. Category TCD is similar to category TBL excluding a cold dome over the high Arctic. The boundary-layer energy-budget patterns are categorized by manually checking case by case if they have the typical characteristics of each categories. Their launch time and launch longitudes are listed in table S1. ~~All ocean sectors fall within either of the~~ WaMAIs over the Kara Ocean sector are characteristic of both ocean sector with land-locked sea ice and open ocean. ~~se, except for the Kara Sea that has some sea ice variability and open ocean. Hence, S~~some WaMAIs behave as typical for the Barents Sea, while some ~~most~~ behave like for the other sectors with land-locked sea ice.

Note that unlike radiation and condensation/evaporation, turbulence does not generate heating/cooling by itself. Instead, it heats/cools air locally by redistributing heat from one altitude to another through mixing within the column. Also, note that the temperature tendencies discussed below are only those that are due to model physics in a Lagrangian view, while in an Eulerian framework, they would be balanced by advection (not shown). In an absolute sense the boundary layer always undergoes a gradual cooling during the advection over the sea ice.

3.3.1 Lifting temperature inversion (INV)

In this category turbulent heating and cooling dominate the boundary-layer energy-budget (Figure 11e and 11h), even though stratocumulus develops along the trajectories and affects the radiative processes (Figure 11a and f). Turbulent mixing transports heat from the upper to the lower parts of the PBL, hence cooling the upper and

warming the lower parts of the PBL (Figure 11h). Since the turbulent mixing persists along the trajectories, the well-mixed layer below the inversion continuously deepens northward (Figure 11b), while the inversion and the cloud top are gradually lifted (Figure 11a). This supports the hypothesis from Tjernström et al. (2019), that the surface inversion formed at the sea ice edge is eroded progressively downstream, by cloud-top cooling and surface turbulent mixing, and eventually the boundary layer must transform into the often observed well-mixed cloud-capped boundary layer (Brooks et al., 2017; Graversen et al., 2008; Morrison et al., 2012; Pithan et al., 2014; Sotiropoulou et al., 2014; Tjernström et al., 2012; Tjernström and Graversen, 2009). Even though this hypothesis was originally posed for summer WaMAIs, it is also applicable to winter WaMAIs over completely frozen ocean sectors; see Figure 15a.

Clouds are relatively thin and radiative cooling near the cloud top is therefore weak (Figure 11f) and only in a few cases the magnitude of radiative cooling is comparable to the turbulent cooling. Generally, in this category, turbulent heating is larger than radiative heating as well as latent heating, and hence boundary-layer warming is dominated by turbulence, but since turbulence only redistribute heat inside the PBL, as a whole it is gradually cooled as the warm air progresses northward.

3.3.2 Radiation-dominated (RAD)

Over the Barents Sea, the maximum air temperature (Figure 12a, 13a, 14a) and specific humidity (Figure 12d, 13d, 14d) over open ocean south of the ice edge are always located right above the sea surface as a result of the strong air-sea interaction and are also typically larger than those over ocean sectors with land-locked sea ice. As this air-mass, considerably affected by air-sea interaction, is advected over the sea ice, different stories take place.

Around 8% of all WaMAIs over the Barents Sea belong to category RAD (Table 2). In this category, the total temperature tendencies are forced by radiative processes. For this category, the large-scale subsidence is an order of magnitude smaller than that in category TBL (Table 3, CONV) and LWP is three times larger than that in category TCD (Table 3, LWP), suggesting that the stratocumulus develops more intensively in category RAD (Figure 12a). With larger values of LWP, longwave radiation is effectively emitted at the cloud top like a black body, exerting large cooling rates with maximum reaching -16 K day^{-1}. However, unlike the cloud formation in category INV, here clouds always already form south of the ice edge over the open water and few clouds develop in the near-surface inversion. In the cloud, heat is redistributed with warming at the cloud top and cooling in the lower PBL by buoyant mixing driven by cloud-top longwave radiative cooling (Figure12h). The turbulent cooling layer in the PBL interior is apparently thicker than the turbulent warming layer whose absolute value of heating rate is considerably more intensive (Figure12h). As shown in figure 12h, the buoyant mixing can access the surface and induce a thicker well-mixed layer below the stratocumulus (Figure 12b). As precipitation constantly erodes the cloud, buoyant mixing continuously provides moisture for the cloud development from the moister air below and hence cloud development as well as the cloud top cooling is maintained.

Meanwhile, the value of maximum temperature and specific humidity is decreasing gradually along the trajectory, indicating that the heat and moisture within the warm-and-moist air is consumed continuously by the cloud formation and surface turbulent mixing. For this category, F_{lw} is comparable to those of category TBL and TCD (Table 3), and increases almost linearly along the trajectory (Figure 16d1) due to the enhancing TWP (Figure 16c1). F_{sh} and F_{lh} are generally smaller than those of category TBL since stronger mixing weakens vertical

334 gradients in the PBL and hence suppresses the surface turbulent heat flux (Table 3). The decreasing rates of F_{sh}

335 and F_{lh} from 0 to 2 degrees north of the sea ice edge are larger than for categories TBL and TCD as a result of

336 stronger buoyant mixing in the PBL (Figure 16a1), while onwards, their decreasing rates are smaller than those

337 for the other two categories since the lifting rates of h_t and h_{sp} are dramatically slowed down (Figure 16b1); see

338 Figure 15b.

3.3.3 Turbulence-dominated (TBL)

340 52% of WaMAIs over the Barents Sea belong to the turbulence dominated category. The variation of surface

341 energy-budget along the trajectory (Figure 16 a2, b2 and c2) is similar to the mean variation of WaMAIs from all

342 categories showed in figure 10c and 10d. Subsidence for WaMAIs in this category is typically a factor of three

343 larger than that in category RAD and it is statistically significantly positive (Table 3, CONV). Consequently,

344 clouds in this category do not develop as intensively as in category RAD and hence the radiative cooling rate at

345 the cloud top is considerably smaller. The boundary-layer energy-budget is mainly dominated by turbulent heating

346 near the surface. As warm-and-moist air is advected into the Arctic sea ice, turbulence exchanges heat between

347 warm and cold air-mass by cooling (heating) warmer (colder) air (Figure 13h), simultaneously inducing a

348 gradually thickening well-mixed layer capped by a strong inversion, and a continuously lifting of h_t and h_{sp} (Figure

349 13b). In this category, the well-mixed layer is substantially thinner than in category RAD, since the turbulent

350 mixing here is mainly forced by surface friction, weaker and less effective than the buoyant mixing in category

351 RAD (Figure 12b). Turbulence is mainly forced by wind shear and buoyancy, but buoyancy is negative here in

352 the initially very stable near-surface layer. Therefore, wind shear mostly fuels the turbulent mixing. In category

353 TBL, turbulent mixing is stronger than in category RAD, but the surface fluxes are still stronger, due to the

354 stronger gradients; F_{sh} and F_{lh} are 77% and 42% larger than those in category RAD. Also see Figure 15c.

3.3.4 Turbulence-dominated with cold dome (TCD)

356 40% of WaMAIs over the Barents Sea belong to this category. For this category, the boundary-layer energy-

357 budget is generally similar to that in category TBL. The main difference is that there is always a layer of cold air

358 (cold dome) laying below the warm-and-moist air-mass especially in the central Arctic (Figure 14c). This cold

359 dome enlarges the vertical temperature gradient and hence intensifies turbulent heat near the surface (Figure 14h).

360 As the warm-and-moist air-mass is advected over the cold dome, it is gradually lifted up by the cold dome and

361 consequently, h_t and h_{sp} are increasing at a faster rate than in category TBL (Figure 16b3). With faster lifting h_t

362 and h_{sp}, F_{sh} and F_{lh} would be reduced more rapidly or even become negative in the high Arctic (Figure 16a3).

363 TWP is dominated by LWP in category RAD and TWP is contributed almost equally by LWP and IWP in category

364 TBL, while in category TCD, TWP is gradually more dominated by IWP; the IWP-to-TWP ratio increases linearly

365 from ~50% to ~100% (Figure 16c3); also see Figure 15d.

4. Conclusion

367 Warm Arctic in winter is always related with long-lived blocking (Luo et al., 2017b, 2018). To the west of these

368 blocks, Warm-and-moist air ~~intrusions (WaMAI)~~ is transported to the Arctic, greatly contribut~~ing~~e to Arctic

369 surface warming. In this research, we name these warm events as warm-and-moist air intrusions (WaMAIs). As

370 the persistence of Arctic blocking increases (Luo et al., 2017b), WaMAIs could be more frequent and hence lead

to more amplified Arctic warming in winter (You et al., 2022). To understand the surface and boundary-layer energy-budget as WaMAIs occur, in this paper, we have detected WaMAIs over the Arctic Ocean sectors of Barents, Kara, Laptev, East Siberian, Chukchi and Beaufort Seas in 40 recent winters (DJF from 1979 to 2018) using ERA5 reanalysis. The climatological analysis shows a consistent pattern with a blocking high-pressure system over corresponding ocean sectors leadscontribute to warm-and-moist air intrusions into winter Arctic, supplying moisture for cloud formation, exerting a positive total energy-budget anomaly on the surface.

Statistically, as warm-and-moist air is advected over ocean sectors with land-locked ice cover, such as the Laptev, East Siberian, Chukchi and Beaufort Seas, the longwave irradiance anomaly increases linearly by 2.5 W m^{-2} (degree latitude)$^{-1}$, while the total column cloud liquid water increases linearly by 6 g m^{-2} (degree latitude)$^{-1}$. The longwave irradiance is dominant in the surface energy-budget. We have also analysed the boundary-layer vertical structure along these trajectories, as well as the associated surface energy-budget pattern of over these sectors, and find one main category, elevated lifting temperature inversion (INV), which in structure is similar to summer WaMAIs (You et al., 2021) (Figure 15a).

During WaMAIs over the Barents Sea where open water exists to the south of the sea ice edge, turbulent heat flux is dominant over the surface energy-budget, especially along the first half-way of the trajectories (Figure 10c). This difference on the surface energy-budget between the Barents Sea and frozen sea sectors is also preliminarily discussed by Lee et al. (2017). Three main categories are found; radiation-dominated (category RAD), turbulence-dominated (category TBL) and turbulent-dominated with cold dome (category TCD), comprising 8%, 52% and 40%, respectively, of all WaMAIs. Unlike over the sectors with land-locked sea ice, air-masses over the ice-free Barents Sea are warmed by the sea surface (local process) before being advected over the sea ice (remote process), consequently resulting in more intensive surface warming.

In response to ten times smaller large-scale subsidence, stratocumulus develops more strongly in category RAD with more intensive cloud-top radiative cooling, inducing apparently thicker well-mixed layer (Figure 15b). However, this strong radiative cooling induces intensive buoyant mixing extending from the cloud top till the surface, supresses the surface turbulent mixing and decreases the lifting rate of the height to the maximum temperature (h_t) and to the maximum specific humidity (h_{sp}). Therefore, surface turbulent fluxes in category RAD and the lifting rate of h_t and h_{sp} are apparently smaller than those in category TBL (Figure 15c). With cold dome, less liquid cloud water could be formed and fewer or even negative turbulent fluxes could access to the surface, in comparison with category TBL (Figure 15d). In category TCD, turbulent fluxes decrease faster along the trajectory since warm-and-moist air is lifted to higher altitude above the cold dome (Figure 15d).

Under the background of global warming, the rate of local process has been accelerated by 9% per year (Kim et al., 2019), while the meridional heat and moisture transports (remote processes) over the Barents Sea are also enhanced in recent decades (Nygård et al., 2020). This implies that WaMAI may play a more significant role in the future Arctic warming. Therefore, the potential mechanism which enhances the occurrence and intensity of WaMAI deserves more attentions from atmospheric scientists.

Data availability

All data used can be found on the ERA5 data repository at DOI: www.ecmwf.int/en/forecasts/datasets/reanalysis-datasets/era5.

Author contributions

CY conducted analysis and interpretation of the data under the supervision of MT and AD. CY prepared the original version of the paper. MT and AD provided constructive comments and revisions to the final article.

Competing interests

The authors declare that they have no conflict of interest.

Acknowledgements:

This research was supported by the Swedish Research Council under Grant 2016-03807. The authors are grateful to Cian Woods for providing the trajectory calculation algorithm.

419 **References**

420 Ali, S. M. and Pithan, F.: Following moist intrusions into the Arctic using SHEBA observations in a Lagrangian
421 perspective, Q. J. R. Meteorol. Soc., 146(732), 3522–3533, doi:10.1002/qj.3859, 2020.

422 Andreas, E. L., Guest, P. S., Persson, P. O. G., Fairall, C. W., Horst, T. W., Moritz, R. E. and Semmer, S. R.:
423 Near-surface water vapor over polar sea ice is always near ice saturation, J. Geophys. Res. Ocean., 107(10),
424 doi:10.1029/2000jc000411, 2002.

425 Brooks, I. M., Tjernström, M., Persson, P. O. G., Shupe, M. D., Atkinson, R. A., Canut, G., Birch, C. E.,
426 Mauritsen, T., Sedlar, J. and Brooks, B. J.: The Turbulent Structure of the Arctic Summer Boundary Layer
427 During The Arctic Summer Cloud-Ocean Study, J. Geophys. Res. Atmos., 122(18), 9685–9704,
428 doi:10.1002/2017JD027234, 2017.

429 Cohen, J., Screen, J. A., Furtado, J. C., Barlow, M., Whittleston, D., Coumou, D., Francis, J., Dethloff, K.,
430 Entekhabi, D., Overland, J. and Jones, J.: Recent Arctic amplification and extreme mid-latitude weather, Nat.
431 Geosci., 7(9), 627–637, doi:10.1038/ngeo2234, 2014.

432 Cox, C. J., Stone, R. S., Douglas, D. C., Stanitski, D. M. and Gallagher, M. R.: The Aleutian Low-Beaufort Sea
433 Anticyclone: A Climate Index Correlated With the Timing of Springtime Melt in the Pacific Arctic Cryosphere,
434 Geophys. Res. Lett., 46(13), 7464–7473, doi:10.1029/2019GL083306, 2019.

435 Draxler, R. R.: Sensitivity of a Trajectory Model to the Spatial and Temporal Resolution of the Meteorological
436 Data during CAPTEX, J. Clim. Appl. Meteorol., 26(11), 1577–1588, doi:10.1175/1520-
437 0450(1987)026<1577:soatmt>2.0.co;2, 1987.

438 Gong, T. and Luo, D.: Ural blocking as an amplifier of the Arctic sea ice decline in winter, J. Clim., 30(7),
439 2639–2654, doi:10.1175/JCLI-D-16-0548.1, 2017.

440 Gong, T., Feldstein, S. and Lee, S.: The role of downward infrared radiation in the recent arctic winter warming
441 trend, J. Clim., 30(13), 4937–4949, doi:10.1175/JCLI-D-16-0180.1, 2017.

442 Graham, R. M., Cohen, L., Ritzhaupt, N., Segger, B., Graversen, R. G., Rinke, A., Walden, V. P., Granskog, M.
443 A. and Hudson, S. R.: Evaluation of six atmospheric reanalyses over Arctic sea ice from winter to early summer,
444 J. Clim., 32(14), 4121–4143, doi:10.1175/JCLI-D-18-0643.1, 2019.

445 Graversen, R. G., Mauritsen, T., Tjernström, M., Källén, E. and Svensson, G.: Vertical structure of recent Arctic
446 warming, Nature, 451(7174), 53–56, doi:10.1038/nature06502, 2008a.

447 Graversen, R. G., Mauritsen, T., Tjernström, M., Källén, E. and Svensson, G.: Vertical structure of recent Arctic
448 warming, Nature, 451(7174), 53–56, doi:10.1038/nature06502, 2008b.

449 Hersbach, H., Bell, B., Berrisford, P., Hirahara, S., Horányi, A., Muñoz-Sabater, J., Nicolas, J., Peubey, C.,
450 Radu, R., Schepers, D., Simmons, A., Soci, C., Abdalla, S., Abellan, X., Balsamo, G., Bechtold, P., Biavati, G.,
451 Bidlot, J., Bonavita, M., De Chiara, G., Dahlgren, P., Dee, D., Diamantakis, M., Dragani, R., Flemming, J.,
452 Forbes, R., Fuentes, M., Geer, A., Haimberger, L., Healy, S., Hogan, R. J., Hólm, E., Janisková, M., Keeley, S.,
453 Laloyaux, P., Lopez, P., Lupu, C., Radnoti, G., de Rosnay, P., Rozum, I., Vamborg, F., Villaume, S. and

454   Thépaut, J. N.: The ERA5 global reanalysis, Q. J. R. Meteorol. Soc., 146(730), 1999–2049,

455   doi:10.1002/qj.3803, 2020.

456   Kim, B. -M., Son, S. -W., Min, S. -K., Jeong, J. -H., Kim, S. -J., Zhang, X., Shim, T. and Yoon, J. -H.:

457   Weakening of the stratospheric polar vortex by Arctic sea-ice loss, Nat. Commun., 5, doi:10.1038/ncomms5646,

458   2014.

459   Kim, K. -Y. and Son, S. -W.: Physical characteristics of Eurasian winter temperature variability, Environ. Res.

460   Lett., 11(4), doi:10.1088/1748-9326/11/4/044009, 2016.

461   Kim, K. -Y., Kim, J. -Y., Kim, J., Yeo, S., Na, H., Hamlington, B. D. and Leben, R. R.: Vertical Feedback

462   Mechanism of Winter Arctic Amplification and Sea Ice Loss, Sci. Rep., doi:10.1038/s41598-018-38109-x,

463   2019.

464   Komatsu, K. K., Alexeev, V. A., Repina, I. A. and Tachibana, Y.: Poleward upgliding Siberian atmospheric

465   rivers over sea ice heat up Arctic upper air, Sci. Rep., 8(1), doi:10.1038/s41598-018-21159-6, 2018.

466   Lee, S., Gong, T., Feldstein, S. B., Screen, J. A. and Simmonds, I.: Revisiting the Cause of the 1989–2009

467   Arctic Surface Warming Using the Surface Energy Budget: Downward Infrared Radiation Dominates the

468   Surface Fluxes, Geophys. Res. Lett., 44(20), 10,654-10,661, doi:10.1002/2017GL075375, 2017.

469   Li, M., Luo, D., Simmonds, I., Dai, A., Zhong, L. and Yao, Y.: Anchoring of atmospheric teleconnection

470   patterns by Arctic Sea ice loss and its link to winter cold anomalies in East Asia, Int. J. Climatol., 41(1), 547–

471   558, doi:10.1002/joc.6637, 2021.

472   Lindsay, R., Wensnahan, M., Schweiger, A. and Zhang, J.: Evaluation of seven different atmospheric reanalysis

473   products in the arctic, J. Clim., 27(7), 2588–2606, doi:10.1175/JCLI-D-13-00014.1, 2014.

474   Liu, Y., Key, J. R., Vavrus, S. and Woods, C.: Time evolution of the cloud response to moisture intrusions into

475   the Arctic during Winter, J. Clim., 31(22), 9389–9405, doi:10.1175/JCLI-D-17-0896.1, 2018.

476   Luo, B., Luo, D., Wu, L., Zhong, L. and Simmonds, I.: Atmospheric circulation patterns which promote winter

477   Arctic sea ice decline, Environ. Res. Lett., 12(5), doi:10.1088/1748-9326/aa69d0, 2017a.

478   Luo, D., Yao, Y., Dai, A., Simmonds, I. and Zhong, L.: Increased quasi stationarity and persistence of winter

479   ural blocking and Eurasian extreme cold events in response to arctic warming. Part II: A theoretical explanation,

480   J. Clim., 30(10), 3569–3587, doi:10.1175/JCLI-D-16-0262.1, 2017b.

481   Luo, D., Chen, X., Dai, A. and Simmonds, I.: Changes in atmospheric blocking circulations linked with winter

482   Arctic warming: A new perspective, J. Clim., 31(18), 7661–7678, doi:10.1175/JCLI-D-18-0040.1, 2018.

483   Luo, D., Chen, X., Overland, J., Simmonds, I., Wu, Y. and Zhang, P.: Weakened potential vorticity barrier

484   linked to recent winter Arctic Sea ice loss and midlatitude cold extremes, J. Clim., 32(14), 4235–4261,

485   doi:10.1175/JCLI-D-18-0449.1, 2019.

486   Mayer, M., Tietsche, S., Haimberger, L., Tsubouchi, T., Mayer, J. and Zuo, H. A. O.: An improved estimate of

487   the coupled Arctic energy budget, J. Clim., 32(22), 7915–7934, doi:10.1175/JCLI-D-19-0233.1, 2019.

488 Messori, G., Woods, C. and Caballero, R.: On the drivers of wintertime temperature extremes in the high arctic,
489 J. Clim., 31(4), 1597–1618, doi:10.1175/JCLI-D-17-0386.1, 2018.

490 Mori, M., Watanabe, M., Shiogama, H., Inoue, J. and Kimoto, M.: Robust Arctic sea-ice influence on the
491 frequent Eurasian cold winters in past decades, Nat. Geosci., 7(12), 869–873, doi:10.1038/ngeo2277, 2014.

492 Morrison, H., De Boer, G., Feingold, G., Harrington, J., Shupe, M. D. and Sulia, K.: Resilience of persistent
493 Arctic mixed-phase clouds, Nat. Geosci., 5(1), 11–17, doi:10.1038/ngeo1332, 2012.

494 Nygård, T., Naakka, T. and Vihma, T.: Horizontal moisture transport dominates the regional moistening patterns
495 in the arctic, J. Clim., 33(16), 6793–6807, doi:10.1175/JCLI-D-19-0891.1, 2020.

496 Overland, J. E. and Wang, M.: Recent extreme arctic temperatures are due to a split polar vortex, J. Clim.,
497 29(15), 5609–5616, doi:10.1175/JCLI-D-16-0320.1, 2016.

498 Overland, J. E., Wood, K. R. and Wang, M.: Warm Arctic-cold continents: Climate impacts of the newly open
499 arctic sea, Polar Res., doi:10.3402/polar.v30i0.15787, 2011.

500 Papritz, L.: Arctic lower-tropospheric warm and cold extremes: Horizontal and vertical transport, diabatic
501 processes, and linkage to synoptic circulation features, J. Clim., 33(3), 993–1016, doi:10.1175/JCLI-D-19-
502 0638.1, 2020.

503 Papritz, L., Hauswirth, D. and Hartmuth, K.: Moisture origin, transport pathways, and driving processes of
504 intense wintertime moisture transport into the Arctic, Weather Clim. Dyn., 3(1), 1–20, doi:10.5194/wcd-3-1-
505 2022, 2022.

506 Persson, P. O. G., Fairall, C. W., Andreas, E. L., Guest, P. S. and Perovich, D. K.: Measurements near the
507 Atmospheric Surface Flux Group tower at SHEBA: Near-surface conditions and surface energy budget, J.
508 Geophys. Res. Ocean., 107(10), doi:10.1029/2000jc000705, 2002.

509 Petoukhov, V. and Semenov, V. A.: A link between reduced Barents-Kara sea ice and cold winter extremes over
510 northern continents, J. Geophys. Res. Atmos., doi:10.1029/2009JD013568, 2010.

511 Pithan, F., Medeiros, B. and Mauritsen, T.: Mixed-phase clouds cause climate model biases in Arctic wintertime
512 temperature inversions, Clim. Dyn., 43(1–2), 289–303, doi:10.1007/s00382-013-1964-9, 2014.

513 Pithan, F., Svensson, G., Caballero, R., Chechin, D., Cronin, T. W., Ekman, A. M. L., Neggers, R., Shupe, M.
514 D., Solomon, A., Tjernström, M. and Wendisch, M.: Role of air-mass transformations in exchange between the
515 Arctic and mid-latitudes, Nat. Geosci., 11(11), 805–812, doi:10.1038/s41561-018-0234-1, 2018.

516 Rudeva, I. and Simmonds, I.: Midlatitude winter extreme temperature events and connections with anomalies in
517 the arctic and tropics, J. Clim., 34(10), 3733–3749, doi:10.1175/JCLI-D-20-0371.1, 2021.

518 Screen, J. A. and Simmonds, I.: The central role of diminishing sea ice in recent Arctic temperature
519 amplification, Nature, 464(7293), 1334–1337, doi:10.1038/nature09051, 2010.

520 Screen, J. A., Bracegirdle, T. J. and Simmonds, I.: Polar Climate Change as Manifest in Atmospheric
521 Circulation, Curr. Clim. Chang. Reports, 4(4), 383–395, doi:10.1007/s40641-018-0111-4, 2018.

Sedlar, J. and Tjernström, M.: Clouds, warm air, and a climate cooling signal over the summer Arctic, Geophys. Res. Lett., 44(2), 1095–1103, doi:10.1002/2016GL071959, 2017.

Serreze, M. C. and Francis, J. A.: The arctic amplification debate, Clim. Change, 76(3–4), 241–264, doi:10.1007/s10584-005-9017-y, 2006.

Simmonds, I.: Comparing and contrasting the behaviour of Arctic and Antarctic sea ice over the 35 year period 1979-2013, Ann. Glaciol., 56(69), 18–28, doi:10.3189/2015AoG69A909, 2015.

Simmonds, I. and Li, M.: Trends and variability in polar sea ice, global atmospheric circulations, and baroclinicity, Ann. N. Y. Acad. Sci., 1504(1), 167–186, doi:10.1111/nyas.14673, 2021.

Sotiropoulou, G., Sedlar, J., Tjernström, M., Shupe, M. D., Brooks, I. M. and Persson, P. O. G.: The thermodynamic structure of summer Arctic stratocumulus and the dynamic coupling to the surface, Atmos. Chem. Phys., 14(22), 12573–12592, doi:10.5194/acp-14-12573-2014, 2014.

Stohl, A., Wotawa, G., Seibert, P. and Kromp-Kolb, H.: Interpolation errors in wind fields as a function of spatial and temporal resolution and their impact on different types of kinematic trajectories, J. Appl. Meteorol., 34(10), 2149–2165, doi:10.1175/1520-0450(1995)034<2149:IEIWFA>2.0.CO;2, 1995.

Tang, Q., Zhang, X., Yang, X. and Francis, J. A.: Cold winter extremes in northern continents linked to Arctic sea ice loss, Environ. Res. Lett., doi:10.1088/1748-9326/8/1/014036, 2013.

Tjernström, M. and Graversen, R. G.: The vertical structure of the lower Arctic troposphere analysed from observati0ns and the ERA-40 reanalysis, Q. J. R. Meteorol. Soc., 135(639), 431–443, doi:10.1002/qj.380, 2009.

Tjernström, M., Birch, C. E., Brooks, I. M., Shupe, M. D., Persson, P. O. G., Sedlar, J., Mauritsen, T., Leck, C., Paatero, J., Szczodrak, M. and Wheeler, C. R.: Meteorological conditions in the central Arctic summer during the Arctic Summer Cloud Ocean Study (ASCOS), Atmos. Chem. Phys., 12(15), 6863–6889, doi:10.5194/acp-12-6863-2012, 2012.

Tjernström, M., Shupe, M. D., Brooks, I. M., Persson, P. O. G., Prytherch, J., Salisbury, D. J., Sedlar, J., Achtert, P., Brooks, B. J., Johnston, P. E., Sotiropoulou, G. and Wolfe, D.: Warm-air advection, air mass transformation and fog causes rapid ice melt, Geophys. Res. Lett., 42(13), 5594–5602, doi:10.1002/2015GL064373, 2015.

Tjernström, M., Shupe, M. D., Brooks, I. M., Achtert, P., Prytherch, J. and Sedlar, J.: Arctic summer airmass transformation, surface inversions, and the surface energy budget, J. Clim., 32(3), 769–789, doi:10.1175/JCLI-D-18-0216.1, 2019.

Wang, C., Graham, R. M., Wang, K., Gerland, S. and Granskog, M. A.: Comparison of ERA5 and ERA-Interim near-surface air temperature, snowfall and precipitation over Arctic sea ice: effects on sea ice thermodynamics and evolution, Cryosphere, 13(6), 1661–1679, doi:10.5194/tc-13-1661-2019, 2019.

Woods, C. and Caballero, R.: The role of moist intrusions in winter arctic warming and sea ice decline, J. Clim., 29(12), 4473–4485, doi:10.1175/JCLI-D-15-0773.1, 2016.

556 Woods, C., Caballero, R. and Svensson, G.: Large-scale circulation associated with moisture intrusions into the
557 Arctic during winter, Geophys. Res. Lett., 40(17), 4717–4721, doi:10.1002/grl.50912, 2013.

558 You, C., Tjernström, M. and Devasthale, A.: Warm-Air Advection Over Melting Sea-Ice: A Lagrangian Case
559 Study, Boundary-Layer Meteorol., doi:10.1007/s10546-020-00590-1, 2020.

560 You, C., Tjernström, M. and Devasthale, A.: Eulerian and Lagrangian views of warm and moist air intrusions
561 into summer Arctic, Atmos. Res., 256, doi:10.1016/j.atmosres.2021.105586, 2021.

562 You, C., Tjernström, M., Devasthale, A. and Steinfeld, D.: The role of atmospheric blocking in regulating Arctic
563 warming, Geophys. Res. Lett, 2022. (under review)

564

565

566

567 Table 1. Regional averaged F_{sh}, F_{lh}, F_{sw}, F_{lw} and F_{total} in Kara, Laptev, East Siberian and
568 Beaufort Sea sector. The unit is W m^{-2} for all variables. Statistically significant positive values
569 are in bold.

Sea sector	Barents	Kara	Laptev	East Siberian	Chukchi	Beaufort
F_{sh}	**28.85±16.73**	8.92±13.08	3.17±6.53	6.72±7.77	**13.55±10.87**	5.93 ±8.14
F_{lh}	**10.05±9.83**	0.65±6.58	-0.39±2.19	0.55±2.56	1.56±4.02	0.34±2.19
F_{sw}	-0.024±0.59	-0.077±0.40	-0.029±0.40	-0.16±0.47	-0.095±0.97	-0.077±0.9
F_{lw}	**15.99±14.34**	**16.51±9.93**	5.92±10.88	**15.42±11.16**	**21.77±10.30**	**17.45±10.51**
F_{total}	**54.86±34.41**	**26.01±25.32**	8.67±13.81	**22.52±15.08**	**36.78±16.27**	**23.65±14.85**

570 Table 2. Number of WaMAIs with boundary layer energy budget pattern of category RAD
571 (radiation-dominated), TBL (turbulence-dominated), TCD (turbulence-dominated with cold
572 dome) and INV (lifting temperature inversion), over melting (Barents) and frozen (Laptev,
573 East Siberian, Chukchi and Beaufort) sea sectors.

Sea sector	Melting			Frozen
Category	RAD	TBL	TCD	INV
Number	9	45	33	131

574 Table 3. Averaged F_{sh}, F_{lh}, F_{sw}, F_{lw}, TCLW (from bottom to h_{t_z}; g m^{-2}) and large-scale
575 convergence (CONV; 10^{-5} kg m^{-2} s^{-1}) from category TBL and category RAD. Statistically
576 significant positive values are in bold.

	Category RAD	Category TBL	Category TCD
F_{sw}	-0.0094±0.047	-0.00035±0.0013	-0.0050±0.035
F_{lw}	**31.49±13.96**	**34.61±18.71**	**35.46±13.10**
F_{sh}	**40.99±28.27**	**72.58±40.21**	9.77±23.08
F_{lh}	**17.43±15.42**	**24.79±23.80**	1.02±8.16
TCLW	**96.78±53.31**	**83.11±54.27**	30.13±31.89
CONV	17.19±174.89	**236.05±225.90**	115.00±230.01
Wind Shear	**0.019±0.0061**	**0.026±0.008**	**0.02±0.011**

577

578

579

580
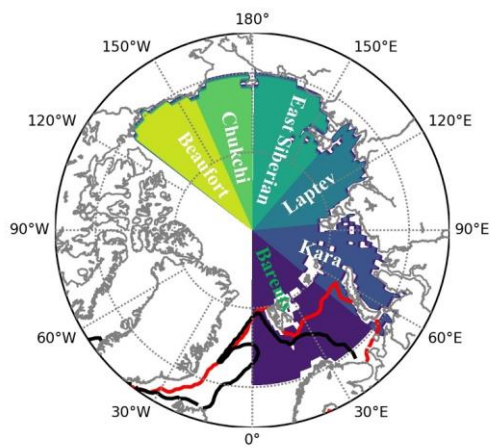
Figure 1. Locations of six sea sectors discussed in this paper, the Barents, Kara, Laptev, East
Siberian, Chukchi and Beaufort Sea sectors. Black line is the mean March sea-ice edge in
1979 and red line is the mean March sea-ice edge in 2015 when the minimum winter sea ice
cover was recorded.
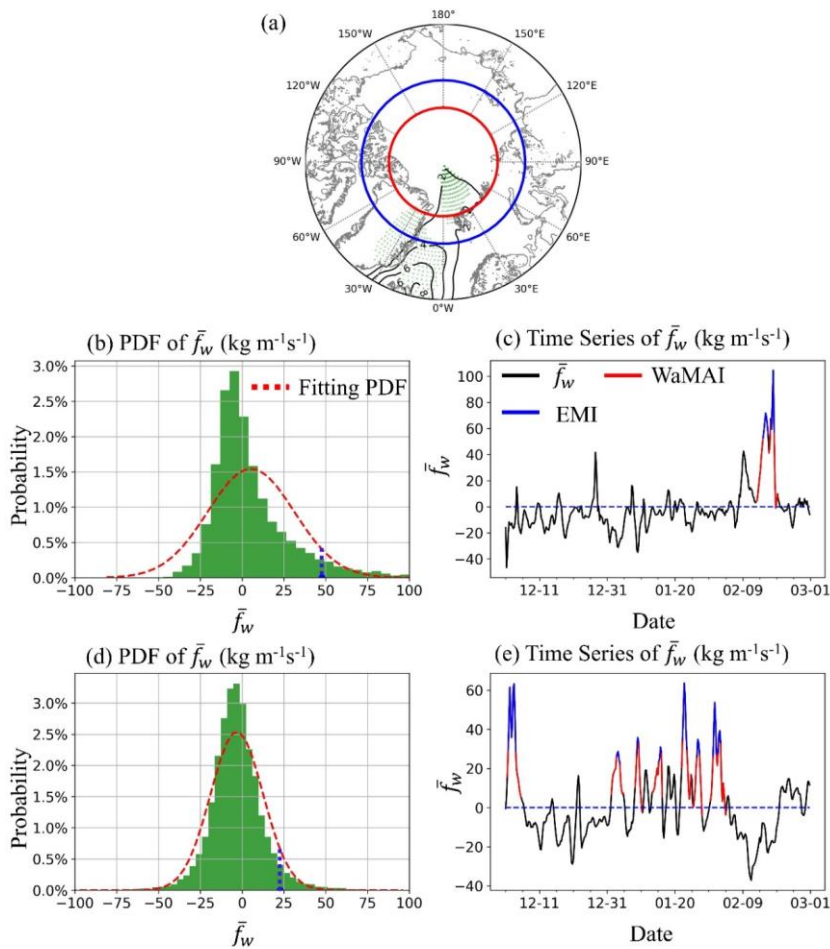
Figure 2. (a) Contours of the linear regrssion~~correlation~~ between local f_w and normalized SIC anomalies (multiplied by -1), defined as the anomaly divided by its standard deviation, for the winter months (DJF) over the Barents Sea. The stippling indicates statistical significance at the $p < 0.05$ level for the Student's t test. Note that the linear regression is calculated against standardized sea ice concentration. Therefore, its unit is same as the unit of f_w and the value represents the general variation of f_w from the climate mean during the sea ice retreat. Red line is the latitude of 80°N where the trajectories over the Barents Sea are launched, while blue line is the latitude of 75°N where the trajectories are launched over the sea sectors of Kara, Laptev, East Siberian, Chukchi and Beaufort; (b) and (d) show the Probability Distribution Function of $\bar{f}_w$ over the Barents and Beaufort Sea, respectively, with the 95-percentile marked as a blue

596 dashed line; (c) and (e) are the time series of $\bar{f}_w$ over the Barents Sea and Beaufort Sea in 1980,

597 respectively, with WaMAI highlighted in red and EMIs highlighted in blue.
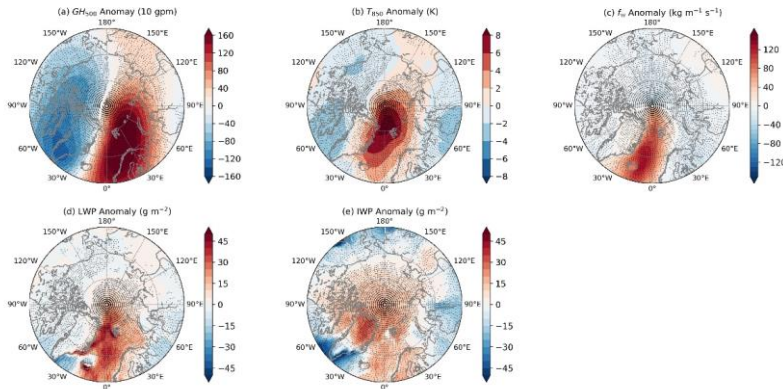
598

599 Figure 3. Composite ERA5 anomalies of (a) 500-hPa GH (10 gpm), (b) 850-hPa temperature
600 (K), (c) northward water-vapor flux ($kgm^{-1}s^{-1}$), (d) liquid water path (g m^{-2}), and (e) ice
601 water path for all EMIs over the Barents Sea, during 1979~2018 winters. The stippling
602 indicates statistical significance at the $p < 0.01$ level from a Student's t test.

603

604
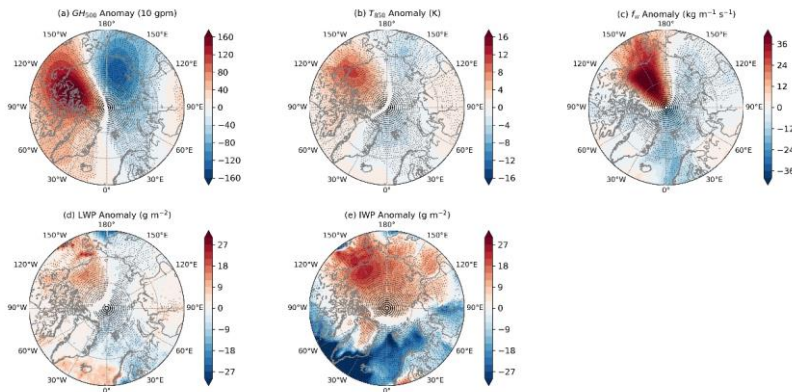
605

606 Figure 4. Composite ERA5 anomalies of (a) 500-hPa GH (10 gpm), (b) 850-hPa temperature
607 (K), (c) northward water-vapor flux ($kgm^{-1}s^{-1}$), (d) liquid water path (g m^{-2}), and (e) ice
608 water path for all EMIs over the Beaufort Sea, during 1979~2018 winters. The stippling
609 indicates statistical significance at the $p < 0.01$ level from a Student's t test.

610
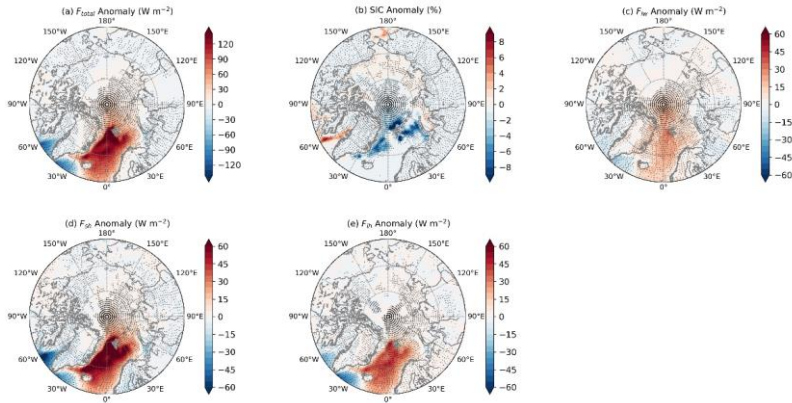
Figure 5. Composite ERA5 anomalies of (a) total surface energy (W m⁻²), (b) sea ice concentration (%), (c) surface thermal net irradiance (W m⁻²), (d) surface sensible heat flux (W m⁻²) and (e) surface latent heat flux (W m⁻²) for all EMIs over the Barents Sea, during 1979~2018 winter. The stippling indicates statistical significance at the $p < 0.01$ level from a Student's t test.
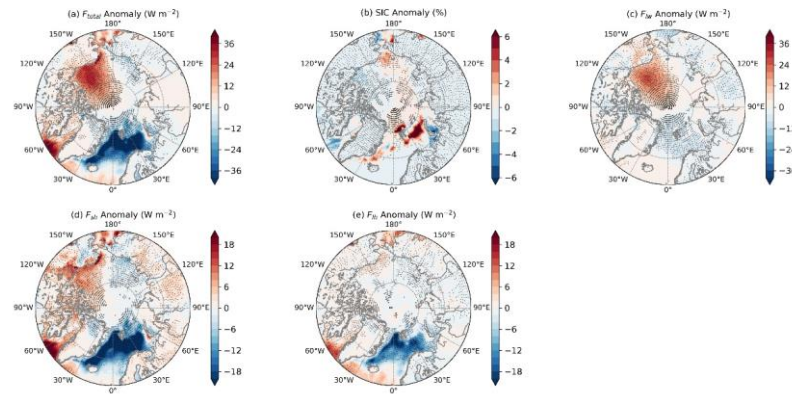
Figure 6. Composite ERA5 anomalies of (a) total surface energy (W m⁻²), (b) sea ice concentration (%), (c) surface thermal net irradiance (W m⁻²), (d) surface sensible heat flux (W m⁻²) and (e) surface latent heat flux (W m⁻²) for all EMIs over the Beaufort Sea, during 1979~2018 winter. Noted that the color-bars here are different than those in figure 5. The stippling indicates statistical significance at the $p < 0.01$ level from a Student's t test.
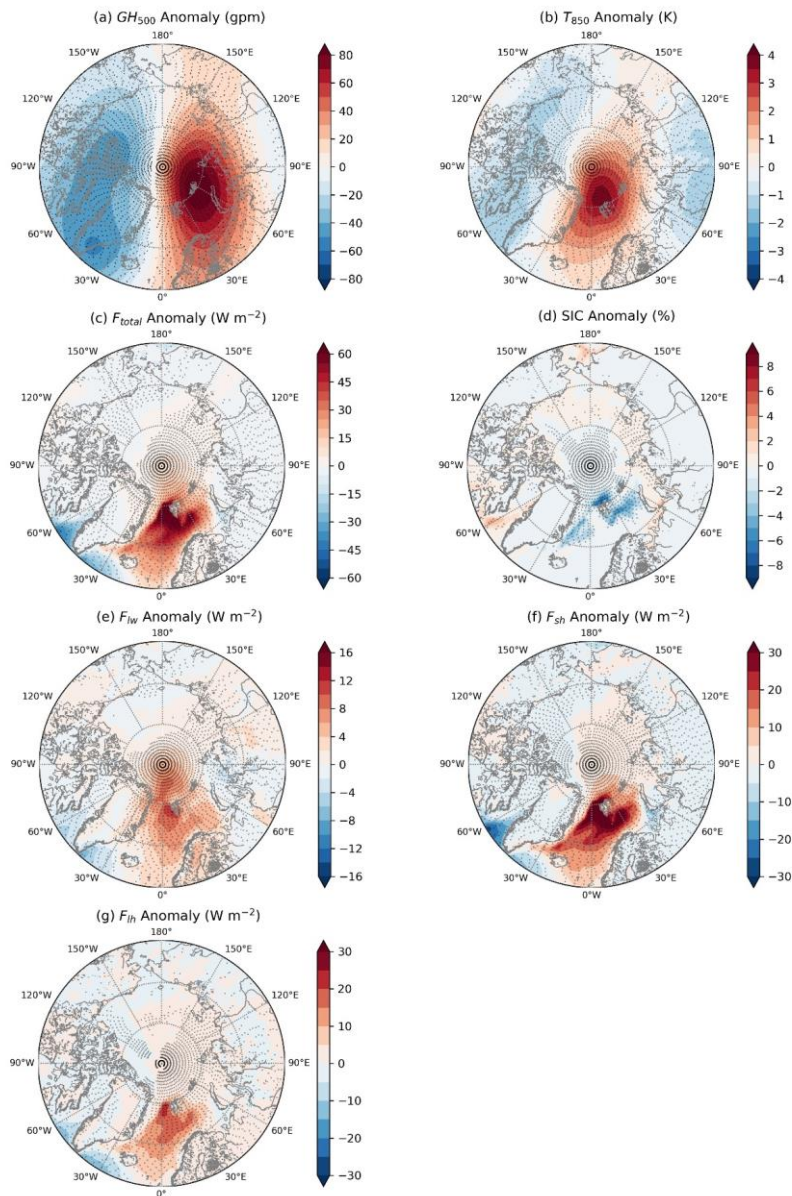
626
627 Figure 7. Anomalies of (a) 500-hPa geopotential height (gpm), (b) 850-hPa temperature (K),
628 (c) F_{total}, (d) SIC, (e) F_{lw}, (f) F_{sh}, and (g) F_{lh} from linear regressions against daily $\bar{f}_w$ time
629 series over the Barents Sea. The stippling indicates statistical significance at the $p < 0.05$ level
630 from a Student's t test.

631

632

633
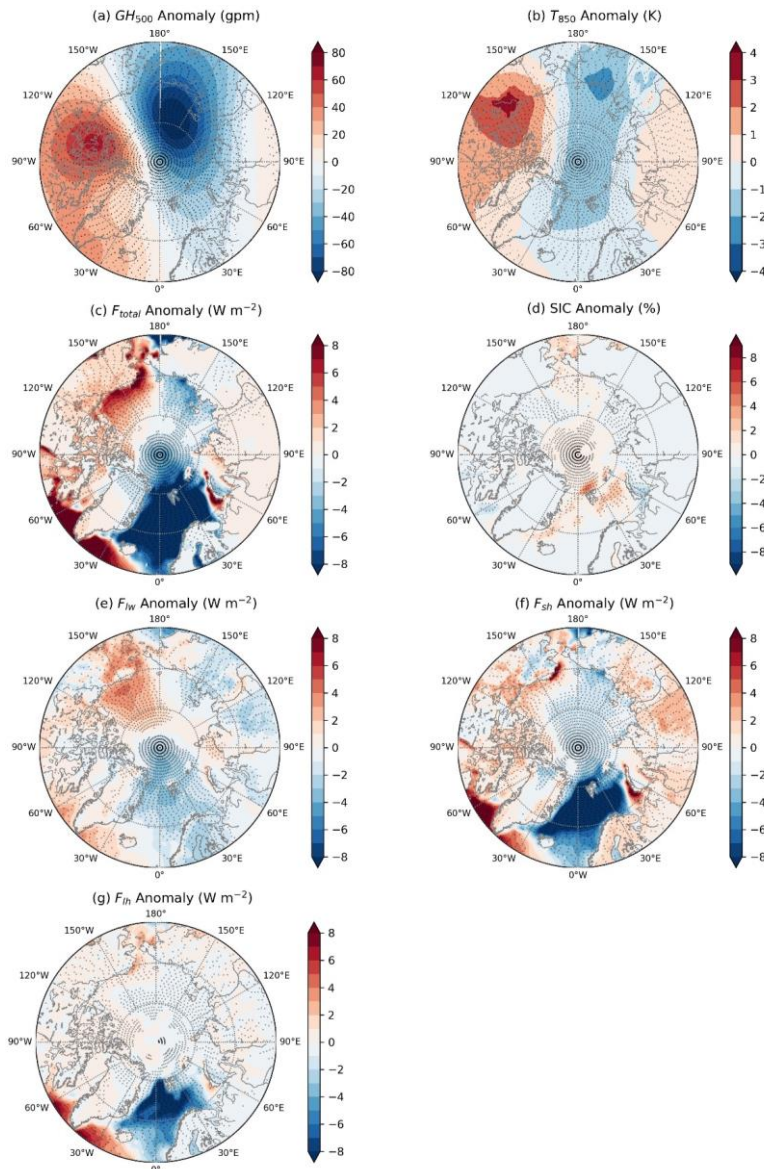
Figure 8. Anomalies of (a) 500-hPa geopotential height (gpm), (b) 850-hPa temperature (K), (c) F_{total}, (d) SIC, (e) F_{lw}, (f) F_{sh}, and (g) F_{lh} from linear regressions against daily $\bar{f}_w$ time series over the Beaufort Sea. The stippling indicates statistical significance at the $p < 0.05$ level from a Student's t test. Similar as figure 2a, the linear regressions here are calculated against standardized f_w. Therefore, the unit of the regression is same as the corresponding

639   variables and the values represent the general anomalies from the climate mean during
640   positive f_w.

641

642
643
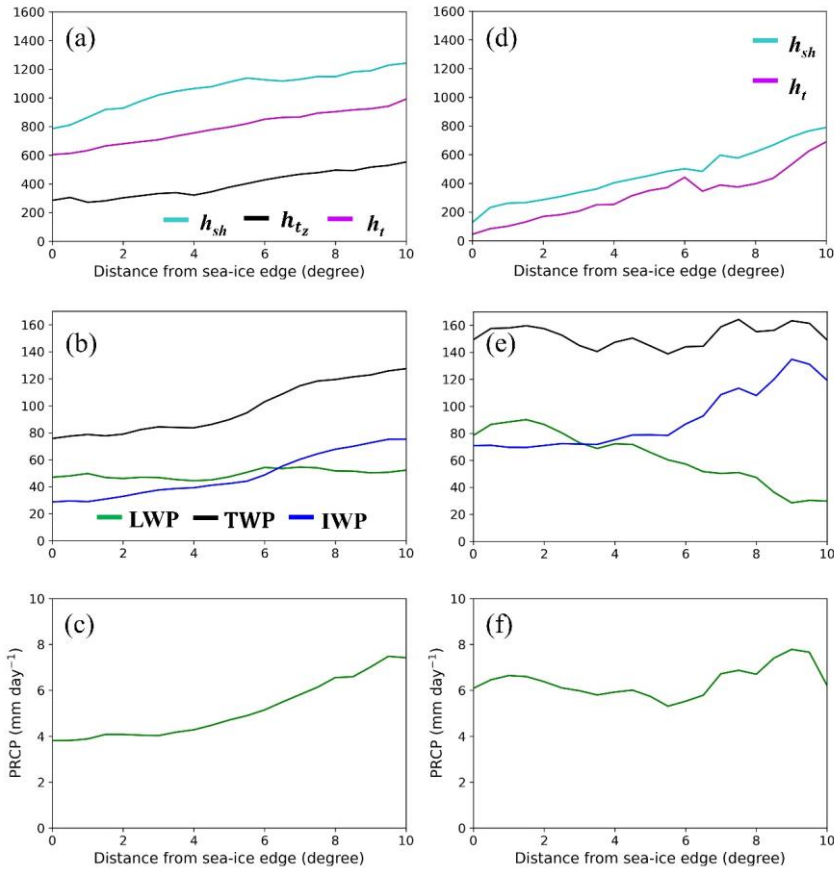
Figure 9: Average variation of (a) the height to the maximum specific humidity (h_{sh}), temperature gradient (h_{t_z}; m) and temperature (h_t); (b) liquid water path (LWP; g m^{-2}), ice water path (IWP; g m^{-2}) and total water path (TWP; g m^{-2}); (c) precipitation rate (PRCP; mm day^{-1}), with the downstream northward distance from sea-ice edge, along the WaMAI trajectories over the Barents Sea. (d) (e) (f) are the counterparts of (a)(b)(c) over the frozen seas. Note that this is not necessarily the distance travelled, since WaMAIs do not need to travel due northward.

651

652

653
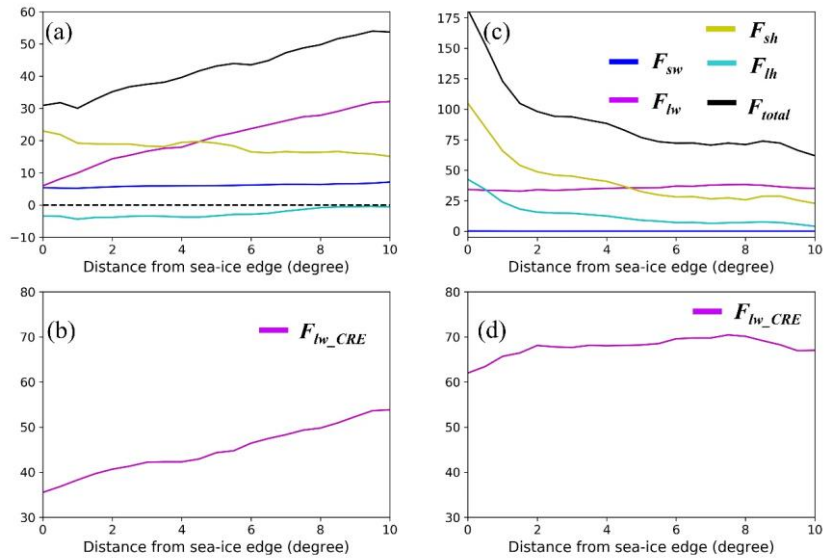
Figure 10. the average meridional evolution in the anomalies of (a) the sum (F_{total}, W m^{-2}; black) and individual surface fluxes of sensible heat (F_{sh}, W m^{-2}; yellow), latent heat (F_{lh}, W m^{-2}; cyan), net longwave irradiance (F_{lw}, W m^{-2}; magenta) and net shortwave irradiance (F_{sw}, W m^{-2}; blue) along the trajectories. (b) shows the cloud radiative effect by longwave (F_{lw_CRE}; magenta) over the Barents Sea. (c)(d) are the counterparts of (a)(b) over the frozen seas.

659
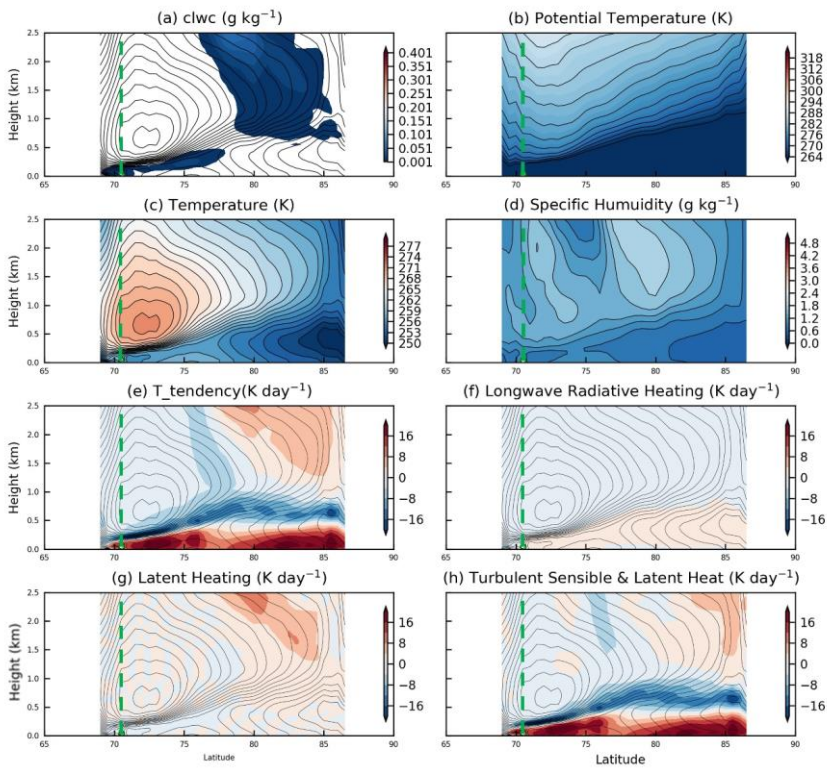
660

661 Figure 11. Latitude-height cross-section of (a) cloud liquid water concentration (g kg⁻¹), (b) potential
662 temperature (K), (c) temperature (K), (d) specific humidity (g kg⁻¹), (e) temperature tendency due
663 to model physics (K day⁻¹), (f) longwave radiative heating (K day⁻¹), (g) latent heating (K
664 day⁻¹) and (h) turbulent heating (K day⁻¹), interpolated from ERA5 along trajectories of one
665 selected WaMAI from category INV. The green dash lines mark the location of ice-edge. See the text
666 for a detailed discussion.

667

668

669
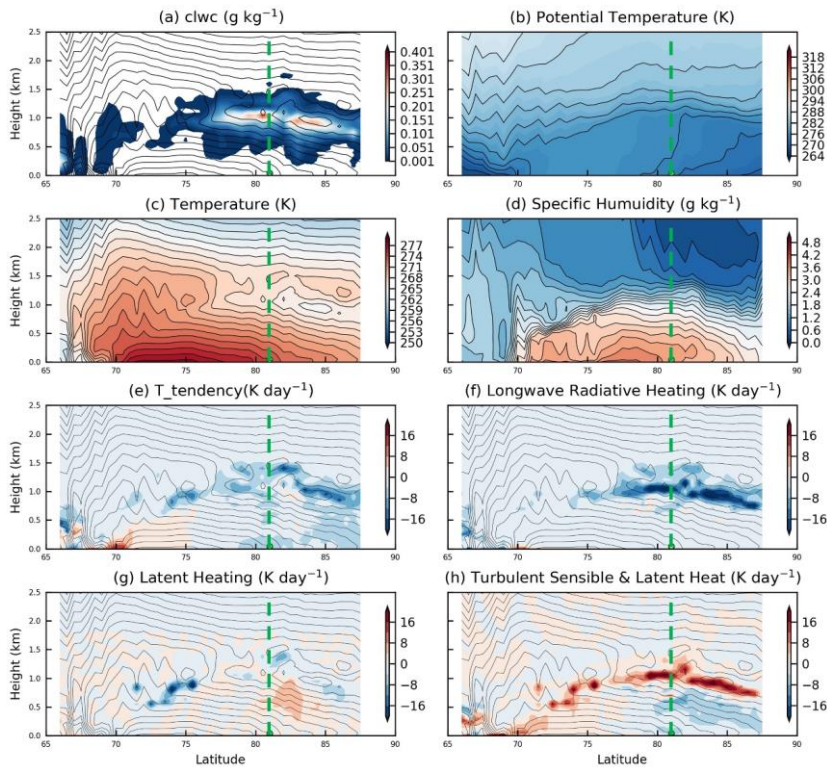
670

671

672   Figure 12. Same as figure 11 but for a selected radiation-dominated WaMAI.

673

674
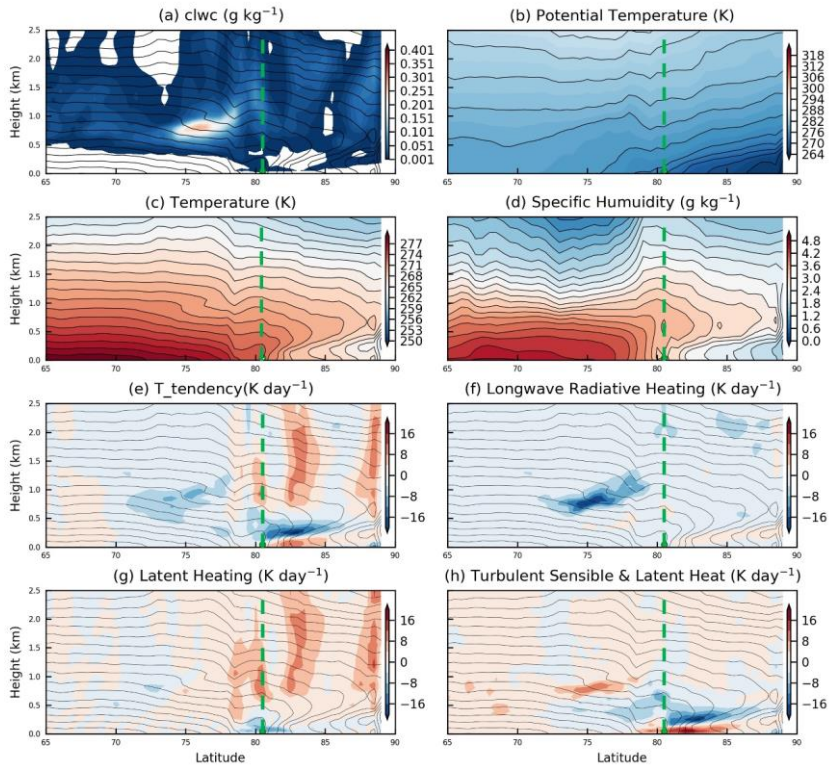
675

676   Figure 13. Same as figure 11 but for a selected turbulence-dominated WaMAI.

677
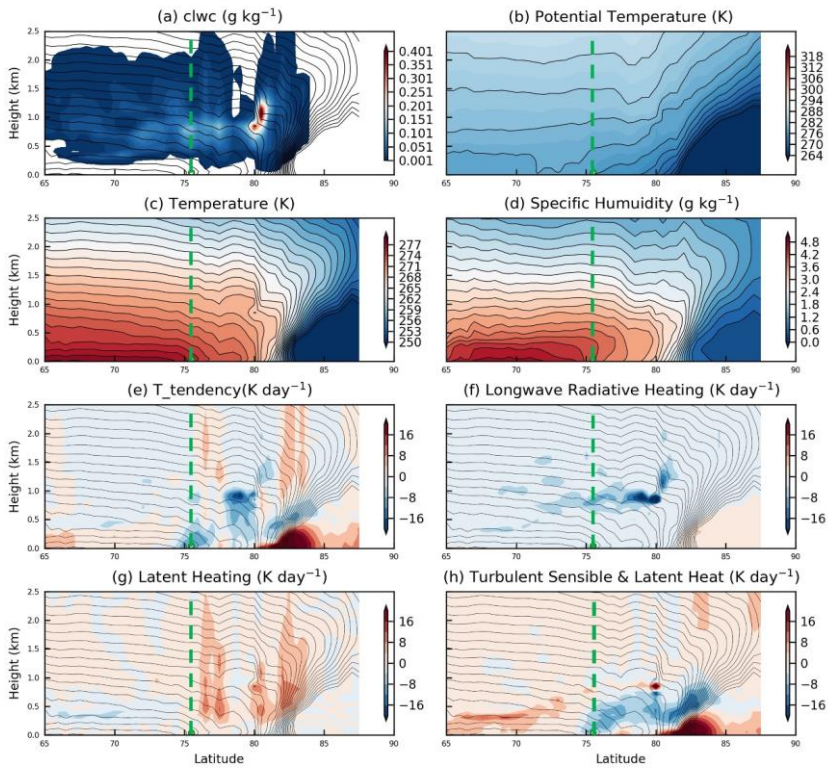
681 Figure 14. Same as figure 11 but for a selected turbulence-dominated WaMAI with cold
682 dome.

684

685
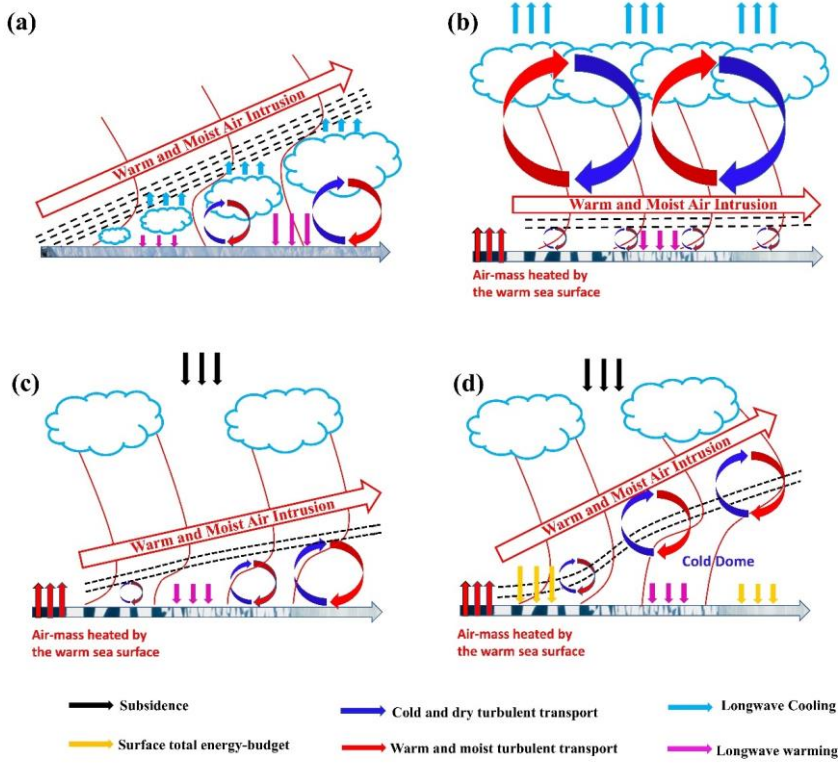
Figure 15. Concept graph of WaMAI from category (a) INV, (b) radiation-dominated
WaMAI, (c) turbulence-dominated WaMAI, (d) turbulence-dominated WaMAI with cold
dome. The red lines in (a)(b)(c) are temperature or humidity profiles. Red arrows represent
the WaMAIs. The horizontal arrows represent the Arctic surface with frozen or melting sea-
ice. Black lines represent inversions.

691
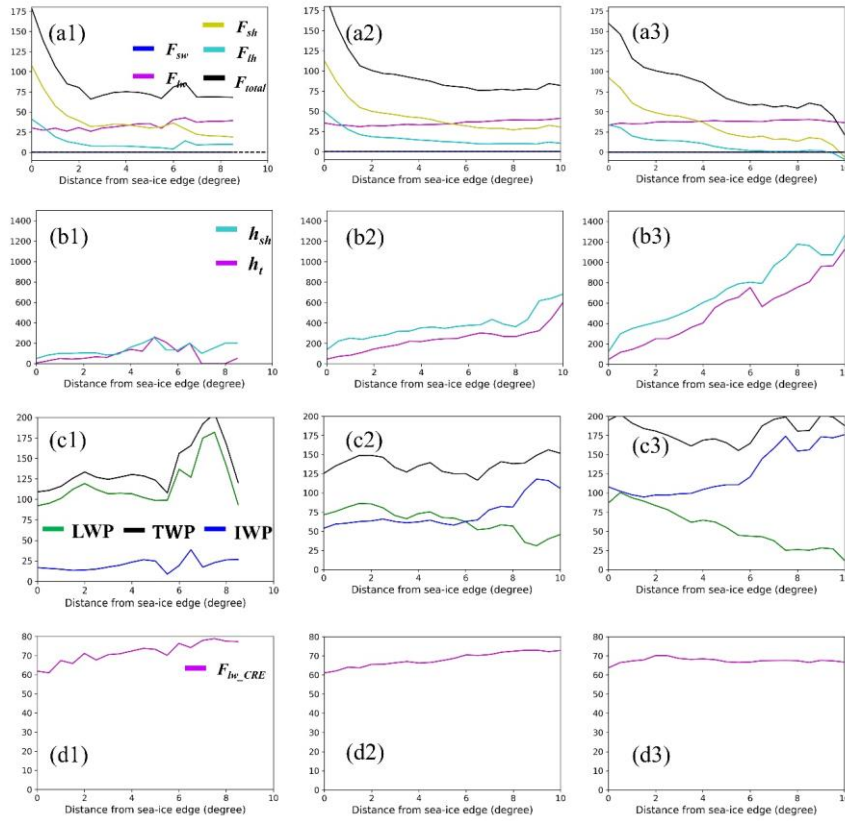
Figure 16. Average variation of (a1) the sum (F_{total}, W m^{-2}; black) and individual surface fluxes of sensible heat (F_{sh}, W m^{-2}; yellow), latent heat (F_{lh}, W m^{-2}; cyan), net longwave irradiance (F_{lw}, W m^{-2}; magenta) and net shortwave irradiance (F_{sw}, W m^{-2}; blue); (b1) the height to the maximum specific humidity (h_{sh}) and temperature (h_t); (c1) liquid water path (LWP; g m^{-2}), ice water path (IWP; g m^{-2}) and total water path (TWP; g m^{-2}); (d1) the cloud radiative effect by longwave (F_{lw_CRE}; magenta), with the downstream northward distance from sea-ice edge, along the trajectory of WaMAI in category of RAD over the Barents Sea. (a2)(b2)(c2)(d2) ((a3)(b3)(c3)(d3)) are the same but for WaMAIs in category of TBL (TCD).